**ROYAL SOCIETY OF CHEMISTRY**

## PAPER

Check for updates

# Intrinsic fluorescence–spin crossover synergy in a 3D Fe(ɪɪ) Hofmann-type framework built from 1,6-dipyridylpyrene and [M$^I$(CN)$_2$]$^-$ (M$^I$ = Ag, Au) bridging ligands

Alejandro Orellana-Silla,[a] Carlos Bartual-Murgui, ID *[b] Gábor Molnár, ID [c] M. Carmen Muñoz ID [d] and José Antonio Real ID *[a]

We report the synthesis, structural characterization, and photophysical investigation of two isostructural 3D Hofmann-type coordination polymers, {Fe$^{II}$(1,6-dipypyr)[M$^I$(CN)$_2$]$_2$)}·(toluene) (1,6-dipypyr = 1,6-dipyridyl-pyrene, M$^I$ = Ag (**1Ag**), Au (**1Au**)), incorporating a pyrene based fluorescent ligand as pillars of the framework. Single crystal X-ray diffraction reveals a primitive cubic (**pcu**) topology formed by square-grid Fe$^{II}$-[M$^I$(CN)$_2$] layers pillared by the 1,6-dipyridylpyrene ligands, with two interpenetrated frameworks stabilized by metallophilic interactions and hosting a disordered toluene molecule. Magnetic and calorimetric measurements demonstrate a complete, reversible two-step spin crossover (SCO) for both compounds. Variable-temperature fluorescence studies show a structured green-yellow emission centered at *ca.* 560–570 nm, bathochromically shifted relative to the free ligand, whose intensity is modulated by the spin-state population. Structural analysis indicates a slipped, edge-to-face arrangement of pyrene units, precluding excimer formation, confirming that the emission is essentially monomeric and directly affected by the coordination environment and spin-state switching. Overall, this work reinforces the concept that intrinsic fluorescence in SCO frameworks provides a robust strategy to design materials with a synergistic fluorescence–SCO response, offering a platform for the rational development of multifunctional spin-switchable systems for sensing and optoelectronic applications.

## Introduction

Pseudo-octahedral Fe$^{II}$ spin crossover (SCO) complexes have a labile electronic configuration reversibly switching between the low-spin (LS, t$_{2g}^6$e$_g^0$) and the high-spin (HS, t$_{2g}^4$e$_g^2$) states under external stimuli such as temperature, pressure, light, and interaction with small molecules (*i.e.* solvents and guests).[1–7] The LS ↔ HS transition involves population/depopulation of the antibonding e$_g$ orbitals and concomitant change in size of the Fe$^{II}$ ionic radius, being *ca.* 0.2 Å smaller in the LS state. In the solid state, this mismatch in size can be transmitted cooperatively from site to site resulting in drastic changes in magnetic, dielectric, calorimetric, optical, structural and elastic properties.[8–13] The possibility of synergistically combining

these SCO features with other interesting properties (*e.g.* fluorescence, conductivity, *etc.*) and the amenability of the SCO compounds to be processed at the micro- and the nano-scale have attracted significant attention in the search for new advanced materials with potential applications in sensors,[14] information storage,[15–17] actuators,[18,19] thermal management[20–28] and spintronics.[29–36]

Among the different families of SCO materials, Fe$^{II}$-Hofmann-type clathrates have emerged as promising candidates due to their tunable frameworks and ability to incorporate multifunctional properties. They are coordination polymers, generically formulated {Fe$^{II}$(L$^{ax}$)$_x$[M(CN)$_y$]$_z$} with M = Ag$^I$, Au$^I$ (*y* = 2; *z* = 2) or Ni$^{II}$, Pd$^{II}$ and Pt$^{II}$ (*y* = 4; *z* = 1) in which the Fe$^{II}$ centers are equatorially connected *via* metallo-cyanato units [M(CN)$_y$]$^{n-}$ (*y* = 2, 4; *n* = 1, 2), forming layered structures. The octahedral geometry of the Fe$^{II}$ sites is axially completed with monodentate terminal (*x* = 2) or bridging bis-monodentate (*x* = 1) pyridine-like[37–39] or triazole-like[40] ligands respectively affording 2D or 3D porous coordination polymers. These materials have been proven to be excellent platforms not only for investigating the influence of guest molecules on the SCO behavior,[41–44] but also for designing multifunctional

[a] *Instituto de Ciencia Molecular, Departamento de Química Inorgánica, Universidad de Valencia, Catedrático José Beltrán 2, 46980 Paterna, Valencia, Spain. E-mail: jose.a.real@uv.es*

[b] *Departamento de Química Física, Universitat de València, Dr Moliner 50, Burjassot, 46100, Spain. E-mail: carlos.bartual@uv.es*

[c] *LCC-CNRS, Université de Toulouse, CNRS, 31077 Toulouse, France*

[d] *Departamento de Física Aplicada, Universitat Politècnica de València, Camino de Vera s/n, 46022, Valencia, Spain*

This journal is © The Royal Society of Chemistry 2026

*J. Mater. Chem. C*, 2026, **14**, 7751–7759 | 7751

materials integrating additional properties such as fluorescence,[45–48] dielectric behaviour,[49] or electrical conductivity,[49–51] among others.

Combining SCO with fluorescence is particularly appealing, as it allows for the optical readout of the spin state, paving the way for innovative sensing applications. Different strategies have been explored to achieve fluorescence in SCO systems, which can be broadly classified into extrinsic[45,46,52–55] and intrinsic[47,56–67] approaches. The extrinsic strategy, based on the incorporation of fluorescent guest molecules into the framework, has proven to be highly effective, as demonstrated in our previous studies. In particular, the use of emissive guests such as pyrene in 3D Hofmann-type networks has enabled efficient spin-state-dependent fluorescence switching, driven by π–π interactions between the guest molecules and the framework pillars. This approach provides significant tunability of optical properties and has opened new avenues for designing SCO-based luminescent materials. On the other hand, the intrinsic strategy, where the fluorescent ligand itself is a coordinating component of the framework, offers a more direct synthetic route to obtaining luminescent SCO materials. This method may ensure a stronger interaction between the SCO centers and the fluorophores, thereby avoiding the need for guest encapsulation. However, the synthesis of intrinsic SCO-fluorescent materials is often more challenging, as it requires the design of multifunctional ligands capable of simultaneously supporting spin transition and luminescence. Despite these challenges, intrinsic systems have shown remarkable results in enhancing the synergy between SCO and fluorescence, providing a robust platform for spin-state optical readout.

In a recent study, we synthesized the first 2D Fe$^{II}$-Hofmann clathrates exhibiting concomitant SCO and fluorescence, further confirming the potential of the intrinsic approach.[47] In these systems, the interplay between fluorescence and SCO was attributed to a resonance effect between the LS-state Fe$^{II}$ d–d absorption band and the excimer/exciplex emission of the organic ligand, leading to temperature-dependent modulation of the fluorescence intensity. These findings reinforced the importance of optimizing the structural arrangement of fluorophores within the lattice to enhance the SCO-fluorescence synergy. More recently, Yan *et al.* reported a 3D Hofmann-type SCO-MOF, {Fe(TPA-dipy)[Ag(CN)$_2$]$_2$}·2EtOH, which exhibits a gradual and incomplete SCO behavior centered at $T_{1/2}$ = 161 K, along with a strong interaction between fluorescence and spin transition.[68] In this system, fluorescence and magnetic-SCO response can be reversibly modulated at low temperatures by alternating irradiation with 532 nm and 808 nm lasers, suggesting its potential application in fluorescence thermometry and photo-switchable materials.

A combination of fluorescence and SCO is not limited to extended systems. Indeed, it has also been explored in mononuclear Fe(II) complexes. For example, Yi *et al.* successfully introduced an aggregation-induced emission (AIE) ligand into a mononuclear Fe$^{II}$ system, obtaining a complex that shows fluorescence increase of up to five times during the spin transition.[69] Moreover, Gao *et al.* synthesized the first

mononuclear Fe$^{II}$ complexes with terminal alkynyl groups, demonstrating a strong correlation between fluorescence intensity and spin-state changes.[70] These studies highlight the versatility of lumino-SCO materials, spanning from extended networks to discrete systems, and underscore the importance of precise molecular design to optimize the interaction between fluorescence and spin transition.

Building upon these advances, here we extend the intrinsic fluorescence strategy designing two new Fe$^{II}$-Hofmann-type compounds incorporating the emissive bridging ligand, 1,6-dipyridylpyrene (1,6-dipypyr). The synthesized compounds, [Fe(1,6-dipypyr)[M(CN)$_2$]$_2$]·(toluene) (M = Au, Ag), exhibit temperature-dependent fluorescence directly linked to their SCO transition. The LS state effectively quenches fluorescence, presumably through the inner filter effect, while the HS state restores luminescence at higher temperatures. This study provides further insight into the mechanisms governing energy transfer in SCO-fluorescent materials and contributes to the rational design of multifunctional spin-switchable systems for optoelectronic and sensing applications.

# Results

## Synthesis

Slow diffusion of a MeOH solution K[M$^I$(CN)$_2$] (M$^I$ = Ag, Au) into a toluene:MeOH (2:1) solution containing 1,6-dipypyr and [Fe(H$_2$O)$_6$(OTs)$_2$] (1:1) afforded yellow crystals of [Fe(1,6-dipypyr)[M(CN)$_2$]$_2$]·(toluene)) [M$^I$ = Ag (1Ag), Au (1Au)] (see the Experimental section). Single crystal, elemental and thermogravimetric (Fig. S1) analyses confirmed that both compounds retain one molecule of toluene per formula. Thermogravimetric analysis shows that the toluene is stable in the framework at room temperature but it is released at temperatures higher than 350 K. Only the crystal structure of the gold solvate has been fully analyzed since the crystals of the silver homologue lack of the necessary quality to be accomplished. However, the X-ray powder diffraction (XRPD, Fig. 1) data confirm that both compounds are isostructural.

## Spin crossover behavior

**Magnetic measurements.** Fig. 2 shows the magnetic properties of **1Ag** and **1Au** expressed as the product of the molar magnetic susceptibility and the temperature, $\chi_M T$, recorded at a temperature rate of 2 K min$^{-1}$ (see the Experimental section). At 350 K the $\chi_M T$ is ca. 3.1 and 3.5 cm$^3$ K mol$^{-1}$ for the silver and gold derivatives, respectively. Upon cooling, $\chi_M T$ remains constant down to ca. 325 K (**1Ag**)/290 K (**1Au**) and, below this temperature, it decreases in a more or less steep fashion in two steps down to a value in the 0.3–0.4 cm$^3$ K mol$^{-1}$ range at 100 K where the LS state dominates. Both extreme values of $\chi_M T$ are consistent with a mostly populated HS and LS state, respectively, in both compounds. The characteristic SCO temperatures, $T_c$, determined as $(\partial \chi_M T/\partial T)$ are $T_{c1}$ = 260/245 K and $T_{c2}$ = 228/190 K, for **1Ag/1Au**. In both cases, no significant hysteresis was observed. In contrast to **1Ag**, the SCO is significantly more
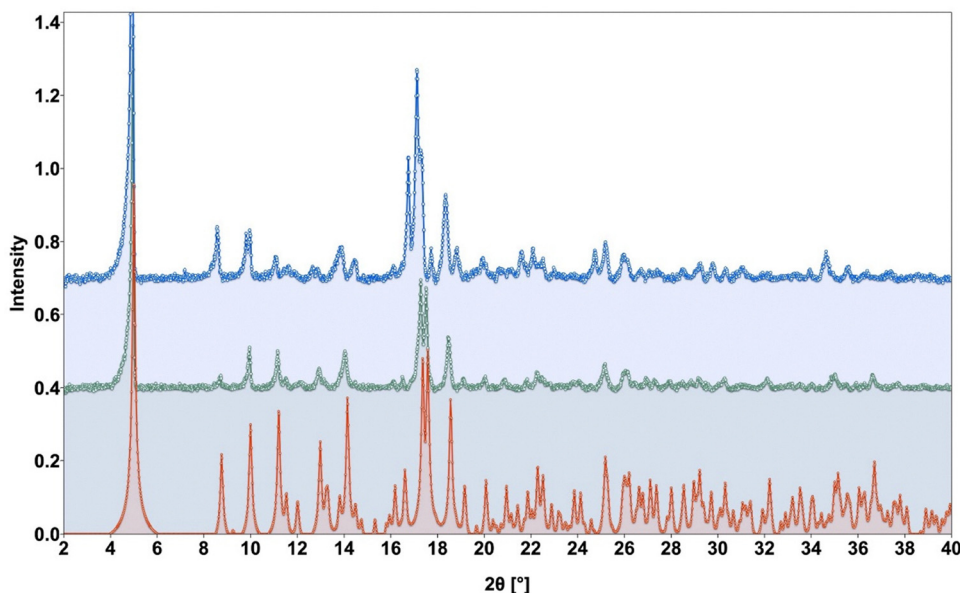
Fig. 1 Powder X-ray diffraction patterns for **1Au** (red: calculated; green: experimental) and **1Ag** (blue).
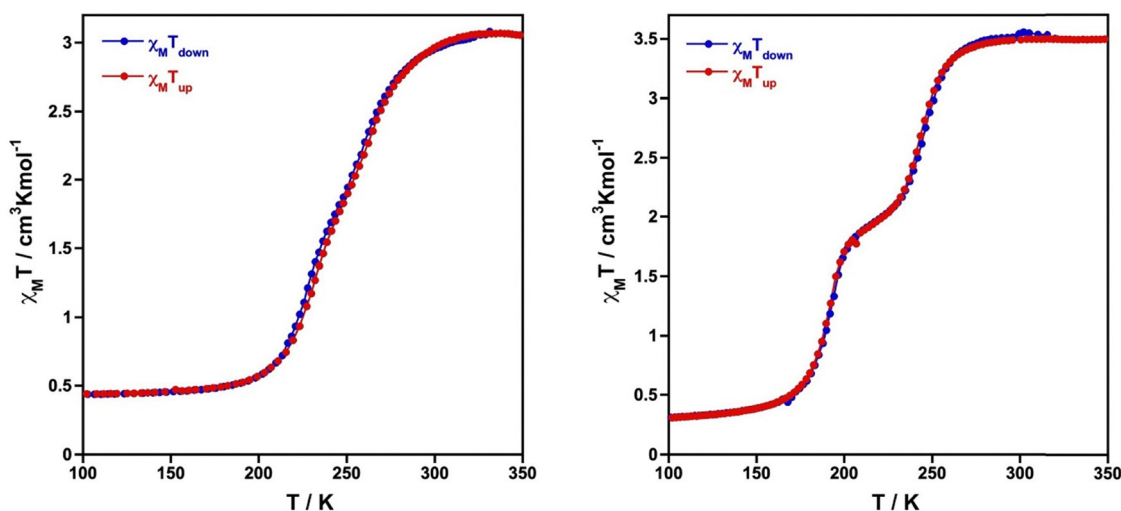


Fig. 2 $\chi_M T$ vs. $T$ plots for **1Ag** (left) and **1Au** right (cooling and heating filled circles correspond to blue and heating modes).

cooperative for **1Au** and in addition both steps are well separated by an inclined plateau of 20 K width. It is worth noting that this magnetic behavior corresponds strictly to the solvent-containing compounds, provided that the samples are not heated above 350 K (see TGA). However, upon heating the samples (400 K for 1 h) in the SQUID chamber, the toluene guest molecules are lost, leading to substantial changes in the magnetic curves. For both the Ag and Au counterparts, the two-step transition becomes a single-step SCO, which is less abrupt and less complete. Moreover, the transition is shifted to lower temperatures for **1Au** (−70 K) and to higher temperatures for **1Ag** (+20 K) with respect to the parent solvated compounds (Fig. S2).

**Differential scanning calorimetry.** Fig. 3 displays the thermal dependence of the molar heat capacity at constant pressure, $\Delta C_p$, obtained from differential scanning calorimetry (DSC), measured at 5 K min$^{-1}$, for **1Ag** and **1Au**. The corresponding $\Delta C_p$ vs. $T$ plots reflect the occurrence of both steps with similar characteristic SCO temperatures to those observed from the $\chi_M T$ vs. $T$ plots. The average enthalpy ($\Delta H$) and entropy, ($\Delta S = \Delta H/T_c^{av}$), variations are 16 kJ mol$^{-1}$ and 67 J K$^{-1}$ mol$^{-1}$ ($T_c^{av}$ = 244.5 K) for **1Ag** and 21 kJ mol$^{-1}$ and 96 J K$^{-1}$ mol$^{-1}$ ($T_c^{av}$ = 218.6 K) for **1Au**.

### Crystal structure

According to the three stable phases observed in the SCO behavior, the structure of **1Au** has been analyzed *via* single crystal X-ray diffraction at 300, 220 and 120 K. In the measured temperature range, the crystals adopt the monoclinic $P2_1/c$
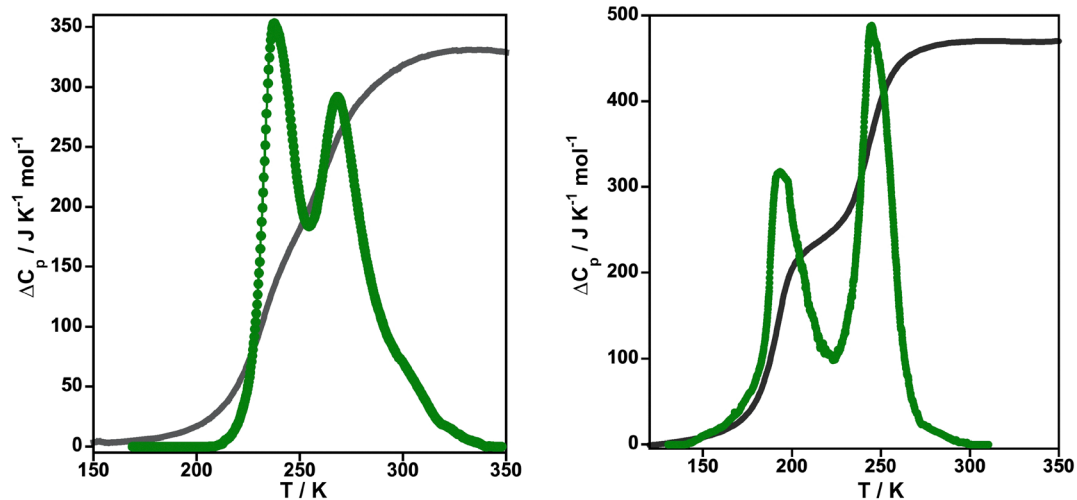
This journal is © The Royal Society of Chemistry 2026

J. Mater. Chem. C, 2026, **14**, 7751–7759 | 7753

Fig. 3 $\Delta C_p$ vs. T plots for **1Ag** (left) and **1Au** right (underlying grey lines correspond to the $\chi_M T$ vs. T plots).

space group. Relevant crystal data are summarized in Table S1. Fig. 4 displays a representative fragment of the structure emphasizing the atom numbering around the Fe$^{II}$ and Au$^I$ centers. The Fe$^{II}$ ion is located at the center of a slightly elongated [Fe$^{II}$N$_6$] octahedron whose equatorial positions are occupied by the N atoms of two crystallographically independent [Au(CN)$_2$]$^-$ and the remaining two axial positions are occupied by the N atom of the pyridine groups of the 1,6-dipypyr ligand. The corresponding metal-to-ligand bond lengths and angles involving the [Fe$^{II}$N$_6$] octahedron are gathered in Table 1 together with relevant geometrical parameters

such as average Fe–N bond length ⟨Fe–N⟩, volume of the octahedron, and angular distortion defined as the sum of the deviation from 90° of the 12 "cis" N–Fe–N angles, $\Sigma = (|\theta - 90|)$. These values are consistent with the HS, LS and intermediate spin state (IM) observed in the thermal dependence of the magnetic properties. The [Au(CN)$_2$]$^-$ groups are practically linear, with the separation from linearity of the N···Au···N angle being 1/2.3° for Au1 and 5.4/7° for Au2, at 300/120 K. They equatorially connect the Fe$^{II}$ centers defining square-grid layers which stack along the b direction and extend parallel to the a–c plane. The layers are separated by the axially coordinated
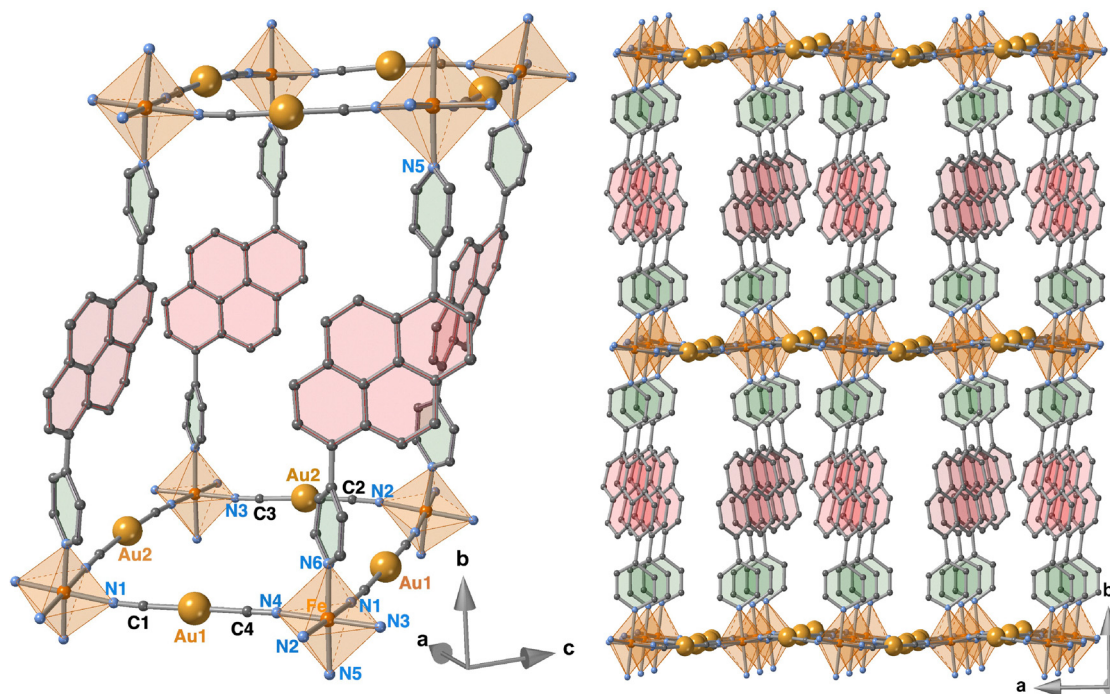


Fig. 4 Fragment of the structure of **1Au** emphasizing the coordination sphere of Fe$^{II}$ and Au$^I$ and the corresponding atom numbering (left). Fragment of the resulting porous metal–organic framework with **pcu** topology (right).

7754 | J. Mater. Chem. C, 2026, **14**, 7751–7759

This journal is © The Royal Society of Chemistry 2026

Table 1 [FeN$_6$] octahedron parameters for **1Au**: Fe–N$_i$ bond lengths, average ⟨Fe–N⟩, volume V$_{[FeN6]}$ and Σ angular distortion (see the text)

| Fe–N$_i$/Å | 300 K | 220 K | 120 K |
|---|---|---|---|
| Fe1–N1 | 2.146(7) | 2.051(10) | 1.964(8) |
| Fe1–N2 | 2.132(6) | 2.041(8) | 1.955(8) |
| Fe1–N3 | 2.140(7) | 2.049(8) | 1.965(8) |
| Fe1–N4 | 2.154(6) | 2.064(10) | 1.976(7) |
| Fe1–N5 | 2.202(6) | 2.117(8) | 2.026(7) |
| Fe1–N6 | 2.184(6) | 2.097(8) | 2.020(7) |
| ⟨Fe–N⟩ | 2.160 | 2.070 | 1.984 |
| V$_{[FeN6]}$/Å$^3$ | 13.380 | 11.870 | 10.434 |
| Σ/° | 14.4 | 14.3 | 11.4 |
| Au1–C1 | 1.989(7) | 1.986(12) | 1.981(10) |
| Au2–C2 | 1.988(8) | 1.984(10) | 1.992(10) |
| Au2–C3 | 2.016(8) | 1.992(11) | 2.002(10) |
| Au1–C4 | 1.974(8) | 1.985(11) | 2.008(10) |
| Au1···Au2 | 3.1379(5) | 3.1161(5) | 3.0897(5) |

1,6-dipypyr ligands affording a porous framework with primitive cubic unit (**pcu**) topology (Fig. 4). The separation between the layers, being 17.536/17.670 Å at 120/300 K favours the interpenetration of an identical framework. Both interpenetrated frameworks are organized in such a way that maximizes the aurophilic interactions between two independent square-grid layers ($d$[Au···Au] = 3.0897(5)/3.1379(5) Å at 120/300 K) (Fig. 5). Despite this interpenetration, there is room for the inclusion of a molecule of toluene, which is positionally disordered in three different positions with an occupancy of 25, 25 and 50% (see Fig. S3).

### Fluorescence properties

The variable temperature emission spectra of compounds **1Au** and **1Ag** are shown in Fig. 6. The photoluminescence was excited at 365 nm, but it is worth noting that similar spectra
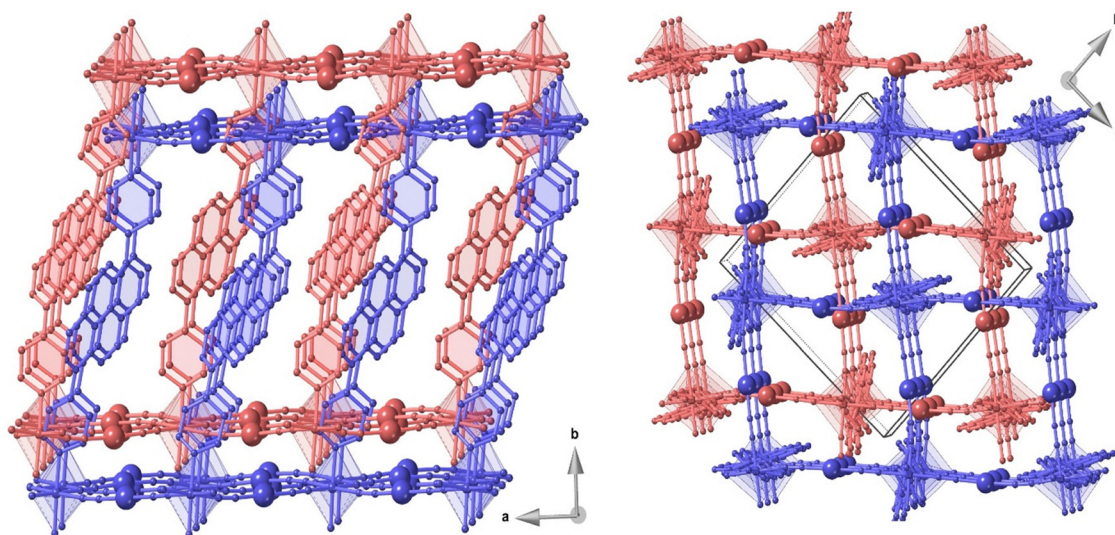


Fig. 5 Two orthogonal views of the interpenetrated frameworks in **1Au** displaying the aurophilic interactions and the accessible void space.
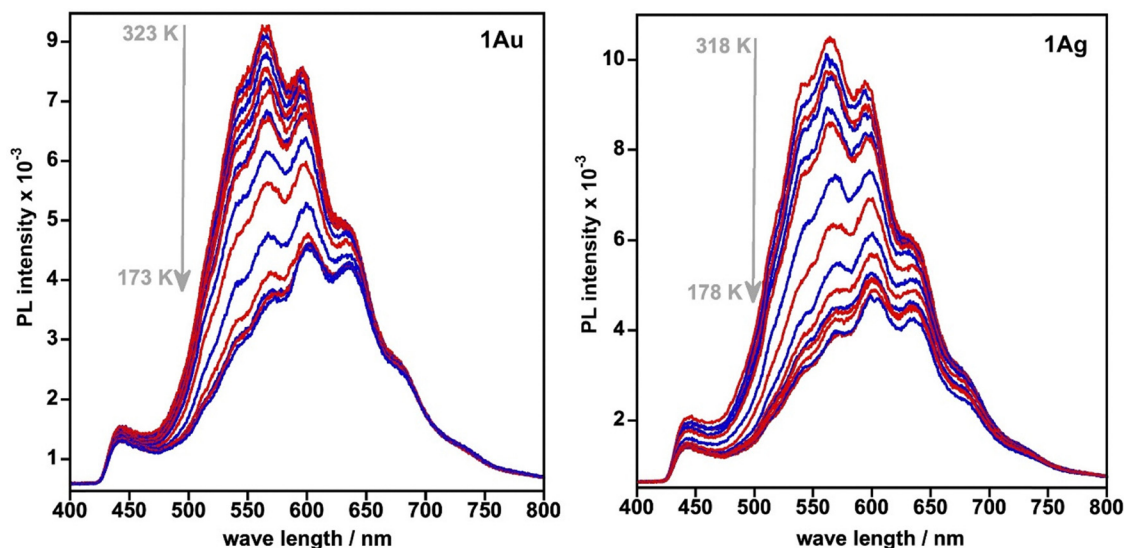


Fig. 6 Variable temperature fluorescence emission spectra recorded for **1Au** and **1Ag** (excitation wavelength: 365 nm).

This journal is © The Royal Society of Chemistry 2026

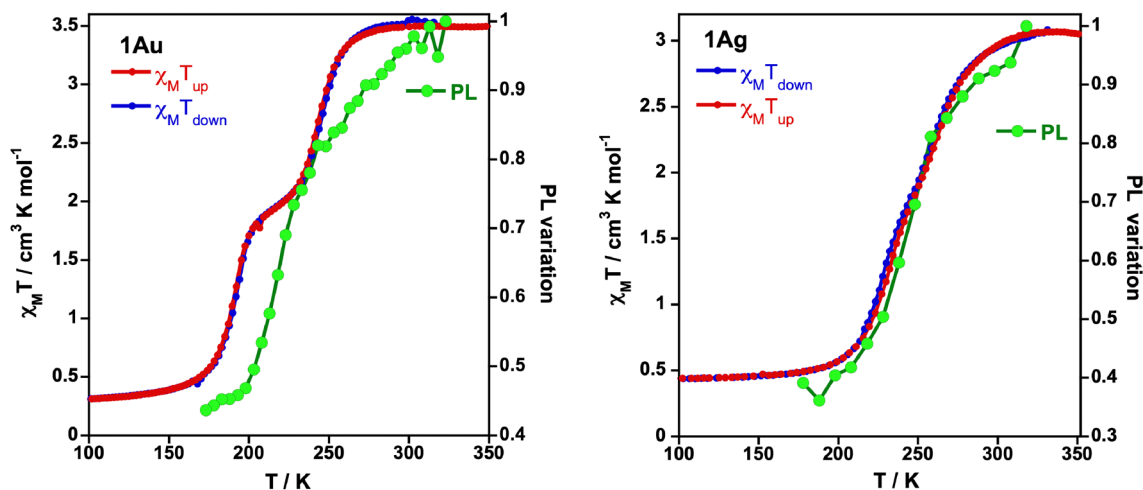J. Mater. Chem. C, 2026, **14**, 7751–7759 | 7755

Fig. 7 Temperature dependence of the photoluminescence (PL) intensity at 550 nm (green circles) for **1Au** and **1Ag** compared to the $\chi_M T$ vs. $T$ plots.

were recorded using other excitation wavelengths between 250 and 450 nm (not shown). The emission spectra of the two compounds are very similar featuring a broad emission centered at *ca.* 565 nm and characterized by a vibronic fine structure. When compared to the luminescence of the pure ligand, either in toluene solution, or in the solid state,[71] the emission in the complexes displays a strong bathochromic shift of *ca.* 150 and 100 nm, respectively, and a significantly better resolved fine structure. Upon cooling the samples from room temperature to *ca.* 170 K, the luminescence intensity drastically decreases by *ca.* 60%, which is just the opposite phenomenon when compared to the ordinary thermal quenching of the luminescence. Besides this unusual decrease of the emission intensity, one can also note a change of the shape of the spectral envelope, with a more pronounced temperature effect at shorter wavelengths. As shown in Fig. 7, the temperature dependence of the luminescence intensity can be clearly correlated with the magnetic behavior of the samples, the correlation being particularly good for **1Ag** and somewhat less tight for **1Au**. The small discrepancy for the latter sample might arise from imperfect sample thermalization in the photoluminescence experiments. Nevertheless, the overall conclusion is clear: when going from the faintly coloured HS state to the deeply coloured LS state, the luminescence intensity suffers a pronounced diminution. Taking into account the magnitude of the change as well as the deformation of the spectral envelope, we can suggest that the luminescence variation with the spin state of the sample is caused by an inner filter effect, *i.e.* by the more efficient reabsorption of the emitted photons in the LS state. This interpretation is further supported by preliminary temperature-dependent luminescence lifetime measurements (Fig. S4), which do not reveal significant changes within experimental uncertainty, indicating that the radiative deactivation pathway of the emitter remains essentially unaffected by the spin state. For a better characterization of this phenomenon, further experiments will be needed, including variable temperature UV-VIS absorption and luminescence lifetime measurements.

## Concluding remarks

In summary, we have successfully synthesized two unprecedented isostructural 3D Hofmann-type coordination polymers made up of a stacking of $\{Fe^{II}(M^I(CN)_2)_4\}_\infty$ ($M^I$ = Ag, Au) grids pillared by the fluorescent 1,6-dipyridylpyrene ligand. The length of both inorganic and organic bridges, favors the interpenetration of two identical frameworks with pcu topology which are coupled to each other *via* metallophilic interactions, a fact that provides room to host a guest toluene molecule. Both compounds are characterized by a structured fluorescent emission band with a maximum centered in the green-yellow window (*ca.* 560–570 nm) which is bathochromically shifted *ca.* 110 nm with respect to the unstructured band shown by the uncoordinated free ligand in the solid state (*ca.* 450–460 nm). The magnetic and calorimetric data confirm that both frameworks exhibit a reversible complete two-step spin crossover behavior. The fluorescence emission of both compounds is clearly modulated by the spin-state switching in the same temperature window. Contrary to what is usual, the intensity of the emission decreases upon cooling. This is due to the increase of the LS population whose light absorption increases significantly in the 400–600 nm window.

In the crystal structure of the free ligand 1,6-dipypyr, each molecule is surrounded by four closest equivalent molecules, defining mutual angles of 39.146° and establishing edge-to-face pyrene–pyrene and pyridine–pyrene C···C contacts in the ranges 3.682–3.830 Å and 3.835–3.976 Å, respectively (with the centroid-to-centroid distance between the pyrene units being 7.092 Å). Consequently, its fluorescence properties are essentially associated with monomeric emission. In the complexes, the 1,6-dipypyr ligands adopt a different organization. At the center of the unit cell there are two parallel 1,6-dipypyr pillars, each belonging to a different framework. The corresponding parallel pyrenes are arranged in a markedly slipped fashion, with their centroids 7.253 Å (120 K) apart, thereby allowing only a few C···C contacts in the 3.8–4.0 Å interval. Additionally, both central pyrenes are related in an edge-to-face manner with two

neighboring pyrenes from the other framework, with a centroid-to-centroid distance of 7.458 Å and a relative angle of 97.665°. This arrangement also permits only a small number of pyrene–pyrene and pyrene–pyridine C···C contacts in the 3.6–3.9 Å range. The absence of strong face-to-face π–π interactions strongly suggests that the emission of the title complexes can also be safely attributed to monomer-like emission.

In light of these structural observations, neither the free ligand nor the interpenetrated frameworks provide packing arrangements capable of promoting significant π–π overlap or excimer formation. This structural evidence, together with the substantial bathochromic shift upon coordination and the spin-state-dependent modulation of the emission, strongly supports that the photophysical properties of the complexes originate from monomer-like pyrene emission whose energy and intensity are governed by the coordination environment and its spin-crossover activity, rather than by excimer- or aggregate-based states. Overall, these results reinforce that intrinsic fluorescence—when the fluorophore is an integral component of the framework—constitutes a robust and reliable design strategy to achieve a genuine synergy between luminescence and spin-crossover behavior, provided that the spin-transition unit is suitably engineered, thereby paving the way toward the obtention of multifunctional materials for sensing and optoelectronic applications.

## Experimental section

### Materials and reagents

$K[M^I(CN)_2]$ ($M^I$ = Au, Ag) and 1,6-di(pyridine-4-yl)pyrene (1,6-dipypyr) were obtained from commercial sources and used without further purification. Hexaquo-iron(II) bis-*p*-toluenesulfonate $[Fe(OH_2)_6(OTs)_2]$ was synthesized as described in the literature.[72]

### Synthesis of 1Ag and 1Au

Fresh crystals of **1Ag** and **1Au** were prepared by a layer-by-layer slow diffusion method in test tubes (yield 60–70%). Yellow crystals were obtained within one week using as precursors 1,6-dipypyr, $[Fe(OH_2)_6(OTs)_2]$ and the corresponding dicyanometallate.

The general procedure for the synthesis is as follows: a solution of $[Fe(OH_2)_6(OTs)_2]$ (0.05 mmol, 25.29 mg) in MeOH (2 mL) is added slowly to a solution of the ligand 1,6-dipypyr (0.05 mmol, 17.82 mg) dissolved in hot toluene (5 mL). After cooling and filtering, the resulting solution is poured into the bottom of a test tube. Then, a buffer mixture of toluene:MeOH (2:1, 5 mL) is added. Finally, a solution of $K[M(CN)_2]$ (M = Au(I)/Ag(I)) (0,1 mmol, 28.81/19.9 mg) in MeOH (2 mL) is poured as the top layer. The test tubes are sealed with a stopper and parafilm and left undisturbed at room temperature. The resulting crystals of **1Ag** and **1Au** were stable under normal conditions without loss of solvent. Elemental analysis for **1Ag** and **1Au**: Calculated for **1Ag** $[C_{37}H_{24}Ag_2FeN_6$ (%)]: C 53.91; H 2.93; N 10.20. Found (%): C 53.75; H 2.95; N 10.04. Calculated for **1Au** $[C_{37}H_{24}Au_2FeN_6$ (%)]: C 44.33; H 2.41; N 8.39. Found (%): C 44.57; H 2.51; N 8.23.

### Physical measurements

**Magnetic measurements.** Variable temperature magnetic susceptibility data were recorded with a Quantum Design MPMS2 SQUID magnetometer equipped with a 7 T magnet, operating at 1 T and at temperatures of 1.8–400 K. Experimental susceptibilities were corrected for diamagnetism of the constituent atoms through the use of Pascal's constants.

**Calorimetric and thermogravimetric measurements.** Differential scanning calorimetry measurements were performed using a Mettler Toledo, Model DSC 821e calorimeter. Low temperatures were obtained with an aluminum block attached to the sample holder, refrigerated with a flow of liquid nitrogen, and stabilized at a temperature of 110 K. The sample holder was kept in a dry box under a flow of dry nitrogen gas to avoid water condensation. The measurements were performed using crystalline samples (~10 mg) of **1Ag** and **1Au** sealed in aluminum pans with a mechanical crimp. Temperature and heat flow calibrations were made with standard samples of indium by using its melting transition (429.6 K, 28.45 J g$^{-1}$). An overall accuracy of ±0.2 K in temperature and ±2% in the heat capacity is estimated. The uncertainty increases for the determination of the anomalous enthalpy and entropy due to the subtraction of an unknown baseline.

Thermogravimetric analysis was performed on a Mettler Toledo TGA/SDTA 851e, in the 290–1200 K temperature range under a nitrogen atmosphere with a rate of 10 K min$^{-1}$.

Variable temperature luminescence emission spectroscopy measurements have been carried out using an Olympus BX51 microscope coupled to a Princeton Instruments Fergie spectrograph, equipped with a back-illuminated CCD sensor, a 50 μm slit and a 295 mm$^{-1}$ grating blazed at 575 nm. Fluorescence was excited at 365 nm (full width at half maximum, FWHM = 9 nm) using a Thorlabs light emitting diode (LED, M365L3). A high-pass filter (>430 nm) was placed before the entrance slit of the spectrograph to block the photons coming from the LED. Temperature control was achieved using a THMS-600 liquid nitrogen cryostage (Linkam Scientific). Variable temperature luminescence lifetime measurements were performed using the time-correlated single photon counting (TCSPC) technique by means of a DeltaFlex (Horiba) instrument equipped with a 303 nm LED (pulse duration 1.2 ns) and a PPD-650 photon counting detector. The temperature was controlled using an Oxford Instruments DN-V liquid nitrogen cryostat. The emission monochromator wavelength was set to 565 nm and a high-pass filter (>500 nm) was placed before the entrance slit of the monocromator to block the photons coming from the excitation light source. Fittings and lifetime calculations were performed using DAS6 fluorescence decay analysis software (Horiba).

**Single crystal X-ray diffraction.** Single-crystal X-ray data were collected on a Nonius Kappa-CCD single crystal diffractometer using graphite monochromated Mo K$_\alpha$ radiation ($\lambda$ = 0.71073 Å). A multi-scan absorption correction was performed. The structures were solved by direct methods using SHELXS-2014 and

This journal is © The Royal Society of Chemistry 2026

*J. Mater. Chem. C*, 2026, **14**, 7751–7759 | **7757**

refined by full-matrix least squares on $F^2$ using SHELXL-2014.[73] Non-hydrogen atoms were refined anisotropically and hydrogen atoms were placed in calculated positions refined using idealized geometries (riding model) and assigned fixed isotropic displacement parameters. CCDC files 2522897, 2522898 and 2522899 contain the supplementary crystallographic data for this article.

## Author contributions

A. O.-S. performed the synthesis and characterization of the complexes (*via* thermal analysis, IR spectra, variable temperature magnetic and calorimetric measurements, and X-ray powder diffraction). C. B.-M. and M. C. M. performed single crystal structure measurements and analysis. G. M. and A. O.-S. determined the thermal dependence of the photoluminescence. J. A. R., M. C. M., C. B.-M. conceived and supervised the project and together with G. M. reviewed and edited the final draft. All authors approved the final version of the manuscript.

## Conflicts of interest

There are no conflicts to declare.

## Data availability

The data supporting the findings of this study, including magnetic, calorimetric and photophysical data, are available within the article and its supplementary information (SI). Supplementary information is available. See DOI: https://doi.org/10.1039/d6tc00153j.

CCDC 2522897–2522899 contain the supplementary crystallographic data for this paper.[74a–c]

## Acknowledgements

## References

1 E. König, *Struct. Bond.*, 1991, **76**, 51–152.
2 J. A. Real, E. Andrés, M. C. Muñoz, M. Julve, T. Granier, A. Bousseksou and F. Varret, *Science*, 1995, **268**, 265–267.
3 P. Gütlich and G. Goodwin, Spin crossover in transition metal compound I−III, *Topics in Current Chemistry*, Springer, Berlin, Heidelberg, Germany, 2004, vol. 233–235.
4 J. A. Real, A. B. Gaspar and M. C. Muñoz, *Dalton Trans.*, 2005, 2062–2079.
5 A. Bousseksou, G. Molnár, L. Salmon and W. Nicolazzi, *Chem. Soc. Rev.*, 2011, **40**, 3313–3335.
6 ed. M. A. Halcrow, *Spin-Crossover Materials: Properties and Applications*, Wiley & Sons, Ltd., 2013.
7 ed. A. Bousseksou, *Spin Crossover Phenomenon*, C. R. Chimie, 2018, vol. 21, pp. 1055–1299.
8 M. A. Halcrow, *Chem. Lett.*, 2014, **43**, 1178–1188.
9 J. A. Real, A. B. Gaspar, V. Niel and V. Muñoz, *Coord. Chem. Rev.*, 2003, **236**, 121–141.
10 B. Weber, W. Bauer and J. Obel, *Angew. Chem., Int. Ed.*, 2008, **47**, 10098–10101.
11 K. S. Kumar, B. Heinrich, S. Vela, E. Moreno-Pineda, C. Bailly and M. Ruben, *Dalton Trans.*, 2019, **48**, 3825–3830.
12 M. Grzywa, R. Röß-Ohlenroth, C. Muschielok, H. Oberhofer, A. Błachowski, J. Żukrowski, D. Vieweg, H.-A. K. von Nidda and D. Volkmer, *Inorg. Chem.*, 2020, **59**, 10501–10511.
13 M. Seredyuk, K. Znovjyak, F. J. Valverde-Muñoz, I. da Silva, M. C. Muñoz, Y. S. Moroz and J. A. Real, *J. Am. Chem. Soc.*, 2022, **144**, 14297–14309.
14 C. Bartual-Murgui, A. Akou, C. Thibault, G. Molnár, C. Vieu, L. Salmon and A. Bousseksou, *J. Mater. Chem. C*, 2015, **3**, 1277–1285.
15 O. Kahn, C. Kröber and C. Jay, *Adv. Mater.*, 1992, **4**, 718–728.
16 O. Kahn and J. Martinez, *Science*, 1998, **279**, 44–48.
17 J. F. Létard, P. Guionneau and L. Goux-Capes, *Top. Curr. Chem.*, 2004, **235**, 221–249.
18 M. D. Manrique-Juarez, S. Rat, L. Salmon, G. Molnar, C. M. Quintero, L. Nicu, H. J. Shepherd and A. Bousseksou, *Coord. Chem. Rev.*, 2016, **308**, 395–408.
19 G. Molnár, S. Rat, L. Salmon, W. Nicolazzi and A. Bousseksou, *Adv. Mater.*, 2018, **30**, 1703862.
20 K. G. Sandeman, *APL Mater.*, 2016, **4**, 111102.
21 P. J. von Ranke, *Appl. Phys. Lett.*, 2017, **110**, 181909.
22 P. J. von Ranke, B. P. Alho, R. M. Ribas, E. P. Nobrega, A. Caldas, V. S. R. de Sousa, M. V. Colaço, L. F. Marques, D. L. Rocco and P. O. Ribeiro, *Phys. Rev. B*, 2018, **98**, 224408.
23 S. P. Vallone, A. N. Tantillo, A. M. dos Santos, J. J. Molaison, R. Kulmaczewski, A. Chapoy, P. Ahmadi, M. A. Halcrow and K. G. Sandeman, *Adv. Mater.*, 2019, **31**, 1807334.
24 K. Ridier, Y. Zhang, M. Piedrahita-Bello, C. M. Quintero, L. Salmon, G. Molnár, C. Bergaud and A. Bousseksou, *Adv. Mater.*, 2020, **32**, 2000987.
25 E. Resines-Urien, M. A. G. García-Tuñón, M. García-Hernández, J. A. Rodríguez-Velamazán, A. Espinosa and J. S. Costa, *Adv. Sci.*, 2022, **9**, 2202253.
26 J. Seo, J. D. Braun, V. M. Dev and J. A. Mason, *J. Am. Chem. Soc.*, 2022, **144**, 6493.
27 M. Romanini, Y. Wang, K. Gürpinar, G. Ornelas, P. Lloveras, Y. Zhang, W. Zheng, M. Barrio, A. Aznar, A. Gràcia-Condal, B. Emre, O. Atakol, C. Popescu, H. Zhang, Y. Long, L. Balicas, J. Lluís Tamarit, A. Planes, M. Shatruk and L. Mañosa, *Adv. Mater.*, 2021, **33**, 2008076.
28 M. Seredyuk, R. Li, K. Znovjyak, Z. Zhang, F. J. Valverde-Muñoz, B. Li, M. C. Muñoz, Q. Li, B. Liu, G. Levchenko and J. A. Real, *Adv. Funct. Mater.*, 2024, 2315487.
29 K. S. Kumar and M. Ruben, *Coord. Chem. Rev.*, 2017, **346**, 176–205.
30 A. Bellec, J. Lagoute and V. Repain, *C. R. Chim*, 2018, **21**, 1287–1299.
31 E. Coronado, *Nat. Rev. Mater.*, 2020, **5**, 87–104.

7758 | *J. Mater. Chem. C*, 2026, **14**, 7751–7759

This journal is © The Royal Society of Chemistry 2026

32 M. Gruber and R. Berndt, *Magnetochemistry*, 2020, **6**, 1–26.

33 K. S. Kumar and M. Ruben, *Angew. Chem., Int. Ed.*, 2021, **60**, 7502–7521.

34 T. K. Ekanayaka, G. Hao, A. Mosey, A. S. Dale, X. Jiang, A. J. Yost, K. R. Sapkota, G. T. Wang, J. Zhang, A. T. N'Diaye, A. Marshall, R. Cheng, A. Naeemi, X. Xu and P. A. Dowben, *Magnetochemistry*, 2021, **7**(3), 37.

35 M. Gavara-Edo, F. J. Valverde-Muñoz, R. Córdoba, M. C. Muñoz, J. Herrero-Martín, J. A. Real and E. Coronado, *J. Mater. Chem. C*, 2023, **11**, 8107–8120.

36 M. Gavara-Edo, F. J. Valverde-Muñoz, M. C. Muñoz, S. E. Moubtassim, F. Marques-Moros, J. Herrero-Martín, K. Znovjyak, M. Seredyuk, J. A. Real and E. Coronado, *Chem. Mater.*, 2023, **35**, 9591–9602.

37 T. Kitazawa, Y. Gomi, M. Takahashi, M. Takeda, M. Enomoto, A. Miyazaki and T. Enoki, *J. Mater. Chem.*, 1996, **6**, 119–121.

38 V. Niel, J. M. Martinez-Agudo, M. C. Muñoz, A. B. Gaspar and J. A. Real, *Inorg. Chem.*, 2001, **40**, 3838–3839.

39 V. Niel, M. C. Muñoz, A. B. Gaspar, G. Levchenko and J. A. Real, *Chem. – Eur. J.*, 2002, **8**, 2446–2453.

40 Y. M. Klein, N. F. Sciortino, F. Ragon, C. E. Housecroft, C. J. Kepert and S. M. Neville, *Chem. Commun.*, 2014, **50**, 3838.

41 Y. Garcia, V. Niel, M. C. Muñoz and J. A. Real, *Top. Curr. Chem.*, 2004, **233**, 229–257.

42 M. C. Muñoz and J. A. Real, *Coord. Chem. Rev.*, 2011, **255**, 2068–2093.

43 R. Ohtani and S. Hayami, *Chem – Eur. J.*, 2017, **23**, 2236–2248.

44 Z.-P. Ni, J.-L. Liu, M. N. Hoque, W. Liu, J.-Y. Li, Y.-C. Chen and M.-L. Tong, *Coord. Chem. Rev.*, 2017, **335**, 28–43.

45 M. Meneses-Sánchez, L. Piñeiro-López, T. Delgado, C. Bartual-Murgui, M. C. Muñoz, P. Chakraborty and J. A. Real, *J. Mater. Chem. C*, 2020, **8**(5), 1623–1633.

46 T. Delgado, M. Meneses-Sánchez, L. Piñeiro-López, C. Bartual-Murgui, M. C. Muñoz and J. A. Real, *Chem. Sci.*, 2018, **9**, 8446–8452.

47 R. Turo-Cortes, M. Meneses-Sánchez, T. Delgado, C. Bartual-Murgui, M. C. Muñoz and J. A. Real, *J. Mater. Chem. C*, 2022, **10**, 10686–10698.

48 Y.-R. Chen, T.-T. Ying, Y.-C. Chen, P.-Y. Liao, Z.-P. Ni and M.-L. Tong, *Chem. Sci.*, 2024, **15**, 9240–9248.

49 N.-T. Yao, L. Zhao, H.-Y. Sun, C. Yi, Y.-H. Guan, Y.-M. Li, H. Oshio, Y.-S. Meng and T. Liu, *Angew. Chem., Int. Ed.*, 2022, **61**, e202208208.

50 F. Lai, L. Getzner, A. Rotaru, G. Molnár, S. Cobo and A. Bousseksou, *Chem. Mater.*, 2025, **37**, 636–643.

51 L. Getzner, D. Paliwoda, L. Vendier, L. M. Lawson-Daku, A. Rotaru, G. Molnár, S. Cobo and A. Bousseksou, *Nat. Commun.*, 2024, **15**, 7192.

52 L. Salmon, G. Molnár, D. Zitouni, C. Quintero, C. Bergaud, J. C. Micheau and A. Bousseksou, *J. Mater. Chem.*, 2010, **20**, 5499–5503.

53 C. M. Quintero, I. A. Gural'skiy, L. Salmon, C. Bergaud, G. Molnár and A. Bousseksou, *J. Mater. Chem.*, 2012, **22**, 3745–3751.

54 I. Suleimanov, O. Kraieva, J. S. Costa, I. O. Fritsky, G. Molnár, L. Salmon and A. Bousseksou, *J. Mater. Chem. C*, 2015, **3**, 5026–5032.

55 H. Shepherd, C. Quintero, G. Molnár, L. Salmon and A. Bousseksou, *Luminescent spin crossover materials in Spin-Crossover Materials: Properties and Applications*, ed. M. A. Halcrow, John Wiley & Sons, 2013, pp. 347–374, ISBN: 978-1-1199-9867-9.

56 B. Benaicha, K. Van Do, A. Yangui, N. Pittala, A. Lusson, M. Sy, G. Bouchez, H. Fourati, C. J. G. S. Triki and K. Boukheddaden, *Chem. Sci.*, 2019, **10**, 6791–6798.

57 J. Yuan, S.-Q. Wu, M.-J. Liu, O. Sato and H.-Z. Kou, *J. Am. Chem. Soc.*, 2018, **140**, 9426–9433.

58 J.-L. Wang, Q. Liu, Y.-S. Meng, X. Liu, H. Zheng, Q. Shi, C.-Y. Duan and T. Liu, *Chem. Sci.*, 2018, **9**, 2892–2897.

59 C. Lochenie, K. Schötz, F. Panzer, H. Kurz, B. Maier, F. Puchtler, S. Agarwal, A. Köhler and B. Weber, *J. Am. Chem. Soc.*, 2018, **140**, 700–709.

60 B. Schäfer, T. Bauer, I. Faus, J. A. Wolny, F. Dahms, O. Fuhr, S. Lebedkin, H.-C. Wille, K. Schlage, K. Chevalier, F. Rupp, R. Diller, V. Schünemann, M. M. Kappes and M. Ruben, *Dalton Trans.*, 2017, **46**, 2289–2302.

61 C.-F. Wang, R.-F. Li, X.-Y. Chen, R.-J. Wei, L.-S. Zheng and J. Tao, *Angew. Chem., Int. Ed.*, 2015, **54**, 1574–1577.

62 Y. Garcia, F.-O. Robert, A. D. Naik, G. Zhou, B. Tinant, K. Robeyns, S. Ebastien Michotte and L. Piraux, *J. Am. Chem. Soc.*, 2011, **133**(40), 15850–15853.

63 M. Hasegawa, F. Renz, T. Hara, Y. Kikuchi, Y. Fukuda, J. Okubo, T. Hoshi and W. Linert, *Chem. Phys.*, 2002, **277**, 21–30.

64 C. Piguet, E. Rivara-Minten, G. Bernardinelli, J.-C. G. Bünzli and G. Hopfgartner, *J. Chem. Soc., Dalton Trans.*, 1997, 421–433.

65 N. Deorukhkar, C. Egger, L. Guénée, C. Besnard and C. Piguet, *J. Am. Chem. Soc.*, 2024, **146**, 308–318.

66 C. Piguet, E. Rivara-Minten, G. Hopfgartner and J.-C. G. Bünzli, *Helv. Chim. Acta*, 1995, **78**, 1651–1672.

67 J.-Y. Ge, Z. Chen, L. Zhang, X. Liang, J. Su, M. Kurmoo and J.-L. Zuo, *Angew. Chem. Int. Ed.*, 2019, **58**, 8789–8793.

68 F.-F. Yan, W.-J. Jiang, N.-T. Yao, P.-D. Mao, L. Zhao, H.-Y. Sun, Y.-S. Meng and T. Liu, *Chem. Sci.*, 2023, **14**, 6936.

69 C. Yi, Y.-S. Meng, L. Zhao, N.-T. Yao, Q. Liu, W. Wen, R.-X. Li, Y.-Y. Zhu, H. Oshio and T. Liu, *CCS Chem.*, 2023, **5**, 915–924.

70 Y. Qu, R. Sun, B.-W. Wang and S. Gao, *CCS Chem.*, 2025, **7**, 2075–2085.

71 Q. Lu, G. K. Kole, A. Friedrich, K. Müller-Buschbaum, Z. Liu, X. Yu and T. B. Marder, *J. Org. Chem.*, 2020, **85**, 4256–4266.

72 S. M. Holmes, S. G. McKinley, G. S. Girolami, P. S. Szalay and K. R. Dunbar, *Inorg. Synth.*, 2002, **33**, 91–103.

73 G. Sheldrick, *Acta Crystallogr. Sect. C*, 2015, **71**, 3–8.

74 (*a*) CCDC 2522897: Experimental Crystal Structure Determination, 2026, DOI: 10.5517/ccdc.csd.cc2qp8sh; (*b*) CCDC 2522898: Experimental Crystal Structure Determination, 2026, DOI: 10.5517/ccdc.csd.cc2qp8tj; (*c*) CCDC 2522899: Experimental Crystal Structure Determination, 2026, DOI: 10.5517/ccdc.csd.cc2qp8vk.

This journal is © The Royal Society of Chemistry 2026

*J. Mater. Chem. C*, 2026, **14**, 7751–7759 | **7759**